Lipoprotein-biomimetic nanostructure enables tumor-targeted penetration delivery for enhanced photo-gene therapy towards glioma

Ruoning Wang [a,b], Xiaohong Wang [b], Junsong Li [b], Liuqing Di [b], Jianping Zhou [a,*], Yang Ding [a,**]

[a] *State Key Laboratory of Natural Medicines, Department of Pharmaceutics, Pharmaceutical University, 24 Tongjiaxiang, Nanjing, 210009, China*
[b] *College of Pharmacy, Jiangsu Provincial TCM Engineering Technology Research Center of High Efficient Drug Delivery System (DDS), Nanjing University of Chinese Medicine, Nanjing, 210023, China*

ARTICLE INFO

ABSTRACT

Glioma is one of the most malignant primary tumors affecting the brain. The efficacy of therapeutics for glioma is seriously compromised by the restriction of blood-brain barrier (BBB), interstitial tumor pressure of resistance to chemotherapy/radiation, and the inevitable damage to normal brain tissues. Inspired by the natural structure and properties of high-density lipoprotein (HDL), a tumor-penetrating lipoprotein was prepared by the fusion tLyP-1 to apolipoprotein A-I-mimicking peptides (D4F), together with indocyanine green (ICG) incorporation and lipophilic small interfering RNA targeted HIF-1α (siHIF) surface anchor for site-specific photo-gene therapy. tLyP-1 peptide is fused to HDL-surface to facilitate BBB permeability, tumor-homing capacity and -site accumulation of photosensitizer and siRNA. Upon NIR light irradiation, ICG not only served as real-time targeted imaging agent, but also provided toxic reactive oxygen species and local hyperthermia for glioma phototherapy. The HIF-1α siRNA in this nanoplatform downregulated the hypoxia-induced HIF-1α level in tumor microenvironment and enhanced the photodynamic therapy against glioma. These studies demonstrated that the nanoparticles could not only efficiently across BBB and carry the payloads to orthotopic glioma, but also modulate tumor microenvironment, thereby inhibiting tumor growth with biosafety. Overall, this study develops a new multifunctional drug delivery system for glioma theranostic, providing deeper insights into orthotopic brain tumor imaging and treatment.

1. Introduction

Glioma is prevalent and deadly primary malignant tumor with high recurrence, poor prognosis and high mortality rate, which accounts for 15% of all brain tumors [1,2]. Enormous efforts and research have been devoted to treating glioma over the last several decades. Because of the blood-brain barrier (BBB), the delivery and penetration of therapeutic agent administration into brain is restricted, resulting in the poor therapeutic effects [3,4]. With the aggravation of glioma condition, BBB is disrupted and referred to the blood-brain-tumor barrier (BBTB). Although the BBTB is more permeable than BBB, the heterogeneous permeability and perfusion of therapeutic drugs are contributed to the suboptimal drug accumulation in brain, which greatly limits the delivery of diagnostic and therapeutic reagents in glioma [5,6]. In addition, the inevitable damage and toxic side effects of glioma resection or therapeutic agents to normal brain tissues are also one of the limiting factors in an effective glioma therapy [7]. Therefore, it is critical to design rationally novel strategies to overcome the biological barriers for effective glioma therapy with improving drug delivery efficiency.

Phototherapy including photodynamic therapy (PDT) and photothermal therapy (PTT) has been developed as new antitumor technologies, owing to the noninvasive feature, high selectivity and low toxicity [8–10]. In this regard, indocyanine green (ICG), the only US FDA-approved and clinically available NIR contrast agent, has demonstrated PDT and PTT activities in recent years due to the remarkable optical features for *in vivo* applications [11]. The light-activated ICG generates toxic reactive oxygen species (ROS) such as singlet oxygen ($^1O_2$) and local hyperthermia, leading to irreversible tumor cell damage even death [12,13]. However, the current restriction of PDT application is due to a high oxygen-dependence and the hypoxic nature of tumor

microenvironment (TME) [14,15]. Hypoxia is a distinct feature in solid tumorigenesis caused by the dysfunction of microvascular systems, and leads to over-activation of hypoxia-inducible factor-1 (HIF-1) for adjusting cellular responses to tissue oxygenation changes [16–18]. Under hypoxia conditions, the oxygen regulated α-subunit dimerizes with β-subunit to form HIF-1, and subsequently initiates downstream gene transcription, such as vascular endothelial growth factor (VEGF), and genes encoding for glucose transporters [19–21]. Collectively, HIF-1α is overexpressed in TME under hypoxia conditions, and induced upregulation of multiple hypoxia responsive transcription enzymes related to tumor progression, proliferation, invasiveness, and metastasis, thereby resulting in dissatisfactory PDT efficacy. Inhibiting the expression of HIF-1α is a unique and alternative way to synergistically improve the antitumor effect for PDT.

RNA interference with high specificity and low toxicity has emerged as a promising modality to revolutionize glioma treatment [22]. Small interfering RNA (siRNA) can be designed to specifically silence expression of any target gene(s), especially those encoding "undruggable" proteins to regulate TME and achieve a desired therapeutic efficacy [23]. Basically, taking HIF-1α as a target to design siRNA (siHIF) could precisely and efficiently knock down the target hypoxia-induced HIF-1α and related protein, thereby improving the glioma TME and enhancing PDT efficacy against glioma. However, there are hurdles for further clinical application in glioma therapy such as extremely short half-life of siRNA in plasma, poor transport across BBB, and rare cellular uptake. For applications, numerous siRNA delivery strategies have been designed to transport siRNA to cells, such as cationic liposomes [24,25], polymeric [26,27] and inorganic nanoparticles [28,29]. Nevertheless, the excessive positive surface charge from cationic materials normally induces systemic toxicity and low selectively *in vivo*, which are still obstacles for efficient siRNA delivery [30]. Therefore, the design of systemic siRNA shuttling strategy to overcome complex biological barriers is urgently needed.

Considerable efforts have been contributed in the last decade to overcome these challenges in brain delivery. Among all, nature opened the bionic door for glioma drug therapy. To increase the tumor site-specificity, red blood cell membranes have been explored to conjugate with antibody or tumor-targeting ligands [31,32]. Moreover, the other studies have utilized exosomes modified with targeting peptides as vehicles to improve the drug-delivery efficiency [33,34]. However, it is particularly difficult to achieve such surface modification through chemical reactions, which would compromise the protein profile of the cell or exosome membrane. High-density lipoproteins (HDLs) afford unique physicochemical properties, including endogenous, inherent biocompatibility, and high penetration through biological barriers, which endow HDL as an effective vehicle for various payloads delivery [35,36]. In recent years, synthetic HDL-mimicking nanoparticles have been widely introduced for drug delivery. These lipoprotein-based nanoparticles shared promising capabilities for targeted delivery to tumor cells through the biologically and functionally similar to endogenous HDLs. One of amphipathic α-helical peptides composed of 18 amino acid residues, D4F (sequence: FAEKFKEAVKDYFAKFWD), a synthetic mimicking peptide of apolipoprotein A-I (apoA-I), has been widely used in various animal disease models [37]. The peptide of D4F retains most of the favorable characteristic properties of endogenous apoA-I while with low immunogenicity. Appositively, free HDL are lacking tumor targeting and penetrating capacity; therefore, an efficient surface modification strategy is necessary. tLyP-1 (CGNKRTRGC) peptide provided with capabilities of tumor homing and cell-penetration, has been proposed to optimize the tissue permeability [38]. The receptor for tLyP-1 was shown to be neuropilin-1 (NRP-1), which is highly expressed on the surface of glioma neovascular endothelial cells and glioma cells [39,40]. Moreover, NRP-1 is also a modular transmembrane protein in neovascularization that mediates drug delivery inside and outside the blood vessels. Thus, the fusion of tLyP-1 with D4F peptides could make delivery vehicle with tumor-homing/penetrating properties

for an important complement to the targeting lesions for efficient delivery.

In this study, we designed a multimodal penetrated HDL fused with penetrating peptide tLyP-1, and high encapsulation of ICG and siRNA, denoted as ptHDL/siHIF-ICG (Fig. 1). The photosensitizer (ICG) is entrapped into hydrophobic core of ptHDL carrier, and the cholesterol-conjugated siRNAs (Chol-siHIF) are fully embedded into the phospholipid monolayer, and protected from enzymatic degradation, thus enabling the nanoparticles meanable for effective photo-gene therapy. The tLyP-1 peptide contains a C-end Rule (CendR)-like sequence, which could bind to NRP-1 receptor on tumor neovascular endothelial cells, facilitating drug diffusion into the extra-vascular tumor parenchyma, as well as penetration into deep tumors [41]. ICG servers as the photo-therapeutic agent to generate not only NIR fluorescence for imaging, but also ROS and local hyperthermia for combined PDT and PTT. Moreover, ptHDL would rapidly collapse from ROS and hyperthermia in TME, resulting in an intracellular burst drug release. The photochemical gene transfection could enhance site-specific release, transfection and silencing efficiency of siHIF, thus inhibiting tumor cell proliferation in hypoxia by downregulating the expression of HIF-1α and VEGF in TME. Therefore, ptHDL/siHIF-ICG is a promising multifunctional nanoplatform to enable *in situ* fluorescence imaging and effective photo-gene therapy.

2. Materials and methods

2.1. Materials

Chol-siNC (Nontargeted control cholesterol-conjugated siRNA, 5′-Chol-UUCUCC GAA CGU GUC ACG UdTdT-3′), and Chol-siHIF (Target sequence, 5′-Chol-AGA GGU GGA UAU GUG UGG GdTdT-3′) were synthesized and purified by Guangzhou Ribo Biotech Co., Ltd. (Guangzhou, China). Apolipoprotein A-I (apoA-I) mimetic polypeptide (D4F, Ac-FAEKFKEAVKDYFAKFWD), tLyP-1 (CGNKRTR), and tLyP-1 fusion D4F (tLyP-1-D4F, Ac-FAEKFKEAVKDYFAKFWD-GSG-CGNKRTR) were synthesized by Anhui Guoping Pharmaceutical Co., Ltd. (Anhui, China). Indocyanine green (ICG) was purchased from Sigma (USA). Soybean phospholipids (PC, purity 90%) were obtained from Shanghai Tywei Pharmaceutical Co., Ltd. (Shanghai, China). DMEM were purchased from Gibco (USA). Trypsin was purchased from Hyclone. Agarose were purchased from Gene TECH Co., Ltd. 2′,7′-dichlorofluorescein diacetate (DCFH-DA) was purchased from Sigma-Aldrich. Singlet Oxygen Sensor Green (SOSG) was purchased from Thermo Fisher Scientific (Waltham, USA). Hypoxia/Oxidative Detection Kit was purchased from Enzo Life Sciences (Switzerland). Annexin V-FITC/PI Apoptosis Detection Kit was obtained from Vazyme Biotech Co., Ltd. (Nanjing, China). All other chemicals in the study were of analytical reagent grade.

2.2. Preparation of ptHDL/siNC-ICG

In order to prepare ptHDL/siNC-ICG, the Lipos/siNC was prepared firstly *via* film dispersion method. In brief, phospholipids were dissolved in organic solvent (chloroform: methanol = 1:1, v/v), and evaporated to form a thin film. DEPC-hydrated lipid membrane containing ICG was added to dissolve the thin film, then sonicated. Chol-siRNA solution (20 μM) was added to the dispersion, then sonicated for 30 min, obtained Lipos/siNC-ICG. The prepared Lipos/siNC-ICG were incubated with different concentrations of peptides (D4F or tLyP-1-D4F) to form rHDL/siNC-ICG and ptHDL/siNC-ICG. The formation of nanoparticles was confirmed by agarose gel electrophoresis. Cy5-ptHDL/Cy3-siNC-ICG, Cy3-Chol-siNC, Cy5-ptHDL, and free ICG were loaded into a 2% agarose gel, which was imaged by the Maestro™-CRi imaging system.
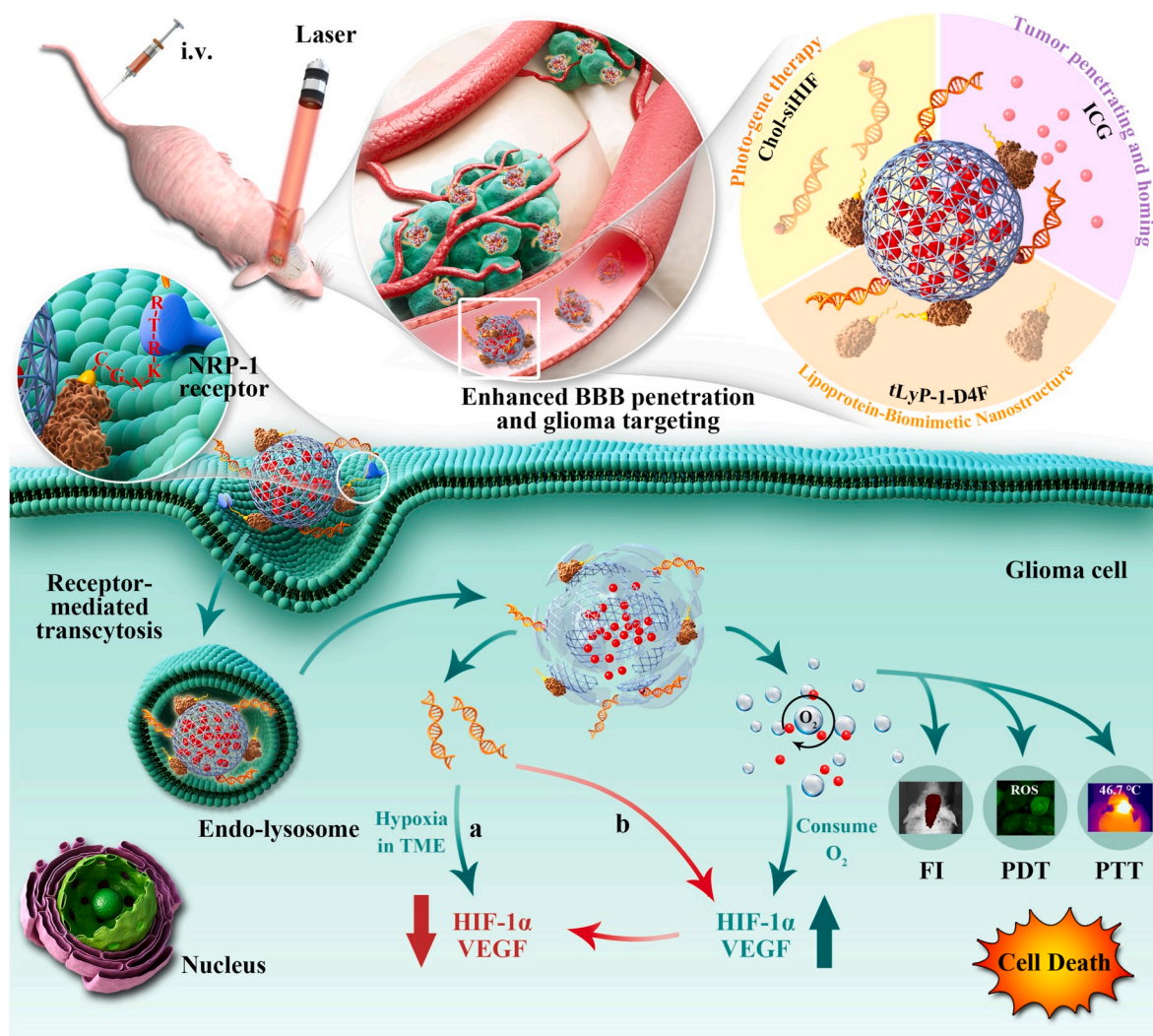
Fig. 1. Schematic illustration of ptHDL/siHIF-ICG and site-specific release for augmenting the FI imaging-guided photo-gene therapy of glioma. ptHDL/siHIF-ICG accumulated in tumor site by targeting peptide-guided tumor-homing routine, and be internalized into glioma cells *via* receptor-mediated endocytosis. ptHDL/siHIF-ICG disassembled in glioma cells upon NIR laser irradiation, and the released ICG serves not only imaging agent but also photosensitizer for phototherapy. (a) Gene siHIF directly downregulate the expression of HIF-1α and VEGF related to TME hypoxia. (b) The PDT effect of ICG consumes oxygen and exacerbates hypoxia condition of TME, thereby inducing upregulation of HIF-1α and VEGF and promoting the function of the gene siHIF.

2.3. Nanoparticle characterization

The particle size, PDI, zeta potential and morphology of ptHDL/siNC-ICG were determined by dynamic light scattering and transmission electron microscopy (TEM). The encapsulation efficiency (EE%) of ICG in the nanoparticles was measured by the formula:

EE (%) = (weight of drugs in nanoparticles/initial weight of drugs) × 100%

The amount of siRNA was measured using a Nano-100 spectrophotometer by detecting free siRNA content after high-speed centrifugation of nanoparticles. The EE (%) of siRNA in the nanoparticles was measured by the formula:

EE (%) = (T[siRNA]- S[siRNA]/ (T[siRNA]) × 100%

ptHDL/siNC-ICG were mixed with serum, and incubated at 37 °C. The results were analyzed by electrophoresis and imaged *via* a GelDoc2000 imaging system. The particle size and PDI were measured at predetermined intervals to confirm the storage stability of pHDL/siNC-ICG.

2.4. Reactive oxygen species (ROS) and singlet oxygen ($^1O_2$) test in vitro

To verify the ROS generation potency, ptHDL/siNC-ICG and free ICG were added to 10 μM of DCFH or SOSG, and irradiated with an 808 nm laser (Meig Waei, China). In a feasible detection procedure, the DCFH was formed after a mixture solution containing methanol solution of DCFH-DA (0.5 mL, 1 mmol/L) and NaOH (2 mL, 0.01 mol/L) was under continuous stirring for 30 min shielded from light. Moderate sodium phosphate buffer (pH = 7) was placed into the above solution to make it to be neutral. The generated ROS and $^1O_2$ were determined by measuring DCF (excitation = 488 nm) and SOG (excitation = 504 nm) fluorescence spectrum. The type of ROS produced by ptHDL/siNC-ICG were tested by an electron spin resonance spectrometer (ESR, E500, Bruker). ESR signals of radicals were trapped by 2,2,6,6-tetramethyl-4-piperidone (TEMPO) and recorded on a Bruker E500 electron paramagnetic resonance spectrometer.

2.5. Photothermal effect of the nanoparticles

To evaluate the *in vitro* photothermal performance, ptHDL/siNC-ICG aqueous solutions at a series of drug concentrations (5, 10, 20, 40 μg/mL

of ICG equivalents) were irradiated by an 808 nm laser (1 W/cm^2) for 5 min. During the irradiation, the temperature of ptHDL/siNC-ICG solution and thermographic images were recorded every 15 s using an infrared thermal camera (Testo 869, Germany), and the AnalyzIR software was used to quantify the temperature from IR thermal images. To investigate the NIR laser power dependent PTT efficiency, 20 μg/mL aqueous solution of ptHDL/siNC-ICG was irradiated under NIR laser of different powers (0.2, 0.5, 0.8, 1.0 and 1.2 W/cm^2), and the temperature was record every 15 s. Besides, to evaluate the photothermal stability, ptHDL/siNC-ICG solution was irradiated and the temperature changes during five consecutive laser on/off cycles were recorded under similar conditions. The photothermal conversion efficiency (η) of ptHDL/siNC-ICG was calculated according to the reported method [42]. The photothermal conversion efficiency (η) was calculated according to Equations (1)–(4):

$$\eta = \frac{hS\Delta Tmax - Qs}{I(1 - A - 808)} \tag{1}$$

$$hS = \frac{mCD}{\tau s} \tag{2}$$

$$t = -\tau_s(\ln\theta) \tag{3}$$

$$Q_s = \frac{mCCD(Tmax(water) - Tsurr)}{\tau water} \tag{4}$$

In which, h represents the heat transfer coefficient, S is the surface area of the sample cell, ΔT_{max} is the temperature difference between the maximum temperature of materials and the surrounding temperature of the environment. Q_s is the heat dissipation from the light absorbed by the solvent and the sample cell. I is the incident laser power (1 W/cm^2), and A^{808} is the absorbance of ptHDL/siNC-ICG at 808 nm m is the mass of the ptHDL/siNC-ICG solution (m = 1 g), C_D is the specific heat capacity of the solvent (C_D = 4.2 -J/g °C). τ_s is the system time constant of ptHDL/siNC-ICG that were calculated to be 172.99 from Fig. 2J, θ is the ratio of ΔT to ΔT_{max}, and t is the cooling time of the sample after irradiation.

2.6. In vitro release

In vitro release of ICG and Chol-siRNA from nanoparticles was detected by dialysis method, and nanoparticles were suspended in PBS buffer (pH 7.4) with or without laser at 1 W/cm^2 a shaking incubator. The supernatant and complexes were periodically collected by centrifugation. The amount of residual siRNA in supernatant was detected using the same analytical method of siRNA-loading efficiency, and the ICG concentration was measured by Elispot Reader.

2.7. Cell culture

U87 cells were cultured in DMEM containing 10% (v/v) FBS, 1% (v/v) penicillin, and 1% (v/v) streptomycin, which were cultured at 37 °C under 5% CO$_2$. The medium was changed every other day.

2.8. In vitro BBB transcytosis

In vitro BBB model was established according to the literature reported before. Briefly, the mouse brain endothelial (bEnd.3) cells were seeded in the upper chamber of 24-well transwell plate and cultured at 37 °C for 7 days. The tight junctions of the bEnd.3 cells monolayer was assessed by detecting the *trans*-endothelial electrical resistance (TEER). Only cell monolayers with TEER greater than 200 Ω were selected for follow-up experiments. U87 cells were cultured in the lower chamber. The Lipos/siNC-ICG, rHDL/siNC-ICG, and ptHDL/siNC-ICG were respectively added to the donor chamber of transwell plate. Competition experiment was carried out by pretreating bEnd.3 cells with free tLyP-1 (100 μg/mL) for 2 h before adding ptHDL/siNC-ICG. The transwells

were then incubated at 37 °C. The permeability of the BBB model was determined by the amounts of nanoparticles in the low chamber. The nanoparticles concentration in the top closet was measured using microplate reader. Transport ratio (%) was calculated as the accumulated amount of the nanoparticles across the monolayer to that of initial amount.

2.9. Cellular uptake of nanoparticles

U87 cells with 1×10^4 cells per well were cultured in the lower chamber of the above BBB model. The nanoparticles labeled with Cy3 and ICG were separately added to the donor chamber of transwell plate. For comparative study, cells were pretreated with excessive tLyP-1 peptide (100 μg/mL) for 0.5 h before incubated with ptHDL/siNC-ICG. After 2 h of incubation, cells were fixed with 4% paraformaldehyde, stained with DAPI (10 μg/mL) for 15 min and observed under confocal laser scanning microscopy (CLSM, LSM 700, Carl Zeiss AG, Germany). For flow cytometry (FACS), cells were washed twice with PBS after incubation and analyzed using flow cytometer (BD Accuri C6, BD Bioscience, USA).

2.10. Penetration of the U87 tumor spheroids

The U87 cells were seeded at a density of 3×10^4 cells per well in 24-well plates coated with 2% (w/v) agarose gel to form the 3D tumor spheroids. The spheroids were cultured with the nanoparticles labeled with Cy3 and ICG. The fluorescence in spheroids was captured with the CLSM using Z-stack with 10 μm intervals. Then, these single-cell suspensions obtained from these spheroids treated with trypsin, were set for flow cytometry analysis.

2.11. Cellular microenvironment assay

Intracellular ROS and hypoxia of ptHDL/siHIF-ICG treated group after laser irradiation were detected by the Hypoxia/Oxidative stress detection kit. The culture and administration of U87 cells were same as described above. Cells were incubated with the kit reagent mix according to the manufacturer's protocols. Then, the cells were washed three times and irradiated under laser. Fluorescent images were captured by CLSM after staining with DAPI. Cells processed as described above were also analyzed using flow cytometry.

### 2.12. Tumor spheroid microenvironment assay

The detection of ROS and hypoxic status in U87 tumor spheroids was the same as 2.11.

2.13. Western bot analysis

CD31 and HIF-1α expression in U87 cells was examined. The cells were then respectively treated with ptHDL/siHIF-ICG, rHDL/siHIF-ICG, Lipos/siHIF-ICG, and ptHDL/siNC-ICG (2 mL 100 nM) under laser. Proteins of cells were isolated by lysis buffer. Immune complexes were formed by incubating primary antibodies (rabbit anti-CD31 and anti––HIF–1α). Finally, the bands were captured with an Odyssey Scanning System.

2.14. In vitro cytotoxicity studies

The *in vitro* cytotoxicity induced by synergistic photo-gene therapy was evaluated by MTT assay. Typically, U87 cells were seeded in 96-well plates at a density of 5×10^3 cells/well and incubated at 37 °C for 24 h. Then, the cells were incubated for 4 h with ptHDL/siNC-ICG (L), Lipos/siHIF-ICG (L), rHDL/siHIF-ICG (L), ptHDL/siHIF-ICG and ptHDL/siHIF-ICG (L) of the same ICG concentration (20 μg/mL), respectively. To induce synergistic photo-gene therapy, each well was irradiated with an
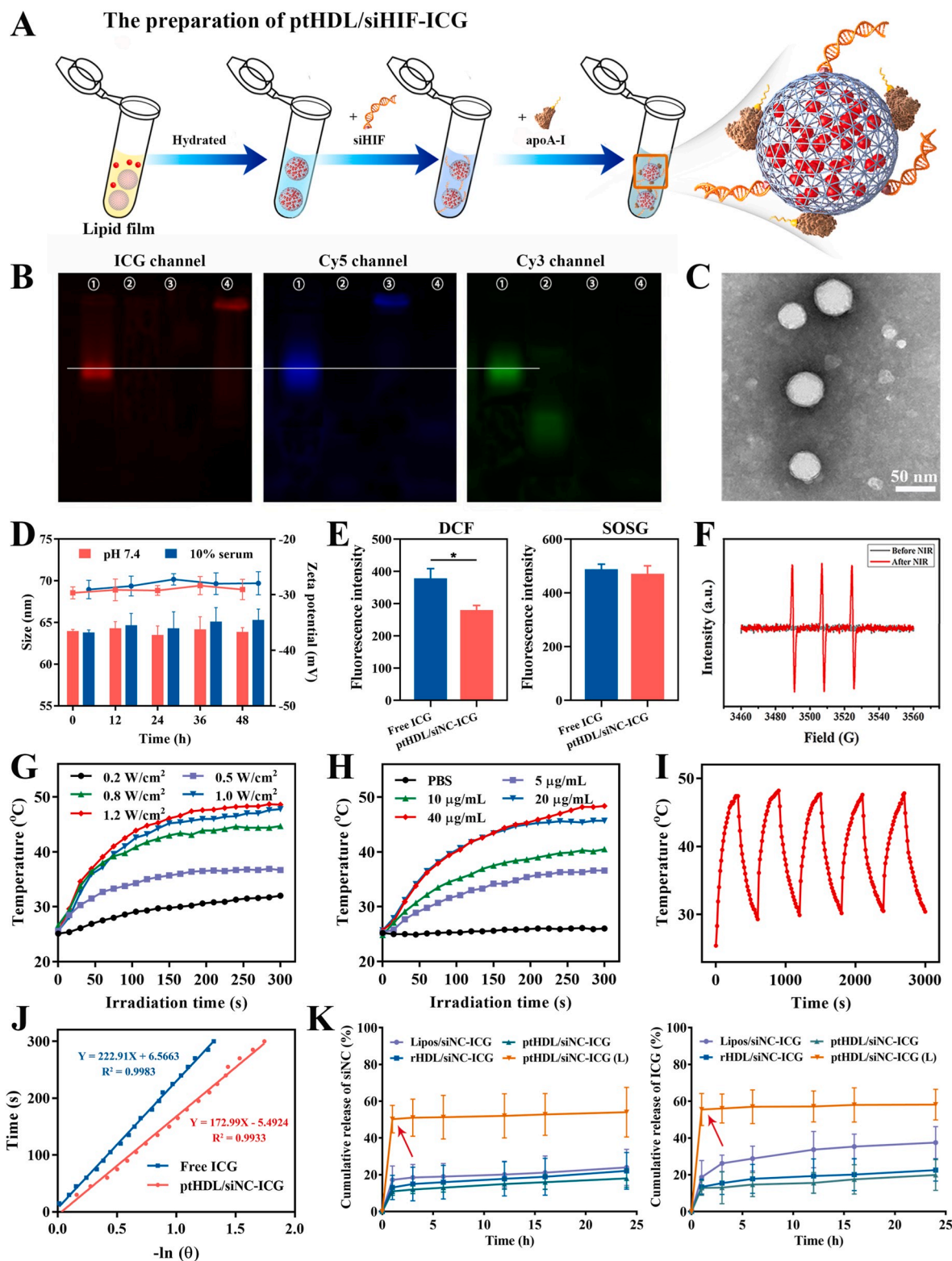
Fig. 2. Characterizations of ptHDL/siNC-ICG. (A) Preparation process of ptHDL/siNC-ICG. (B) Agarose gel electrophoresis was used to confirm the integrity of ptHDL/siNC-ICG. The images represent agarose gel photographed *via* different channels. ptHDL was labeled with Cy5 (blue signal), Chol-siRNA was labeled with Cy3 (green signal), and ICG was in red. Lane ①: Cy5-ptHDL/Cy3-siNC-ICG; lane ②: Cy3-siNC; lane ③: Cy5-ptHDL; lane ④: Free ICG. (C) TEM image of ptHDL/siNC-ICG. Scale bar: 50 nm. (D) Changes in size and zeta potential of ptHDL/siNC-ICG after 48 h of incubation (n = 3). (E) ROS and $^1O_2$ generation of ptHDL/siNC-ICG and free ICG after NIR laser irradiation. (F) ESR spectroscopy detection of ptHDL/siNC-ICG under NIR irradiation. (G) Photothermal conversion of ptHDL/siNC-ICG aqueous solution (20 μg/mL) under 808 nm laser irradiation with different exposure intensity (0.2–1.2 W/cm²). (H) Temperature changes of ptHDL/siNC-ICG solution containing ICG of serial concentration (0–40 μg/mL) after laser irradiation. (I) Photothermal stability study of ptHDL/siNC-ICG aqueous solution (808 nm, 1 W/cm²) during five cycles of on/off laser irradiation processes. (J) Calculation of the time constant (τ_s) by plotting the negative natural logarithm of θ as a function of cooling time for ptHDL/siNC-ICG. (K) The release profiles of Chol-siNC and ICG from different nanoparticles with (ptHDL/siNC-ICG (L)) or without (ptHDL/siNC-ICG) laser *in vitro* (1 W/cm², 5 min), red arrows indicate laser irradiation. (L) stands for "laser". (n = 3, ***p < 0.001).

808 nm laser for 5 min and incubated for 24 h. Thereafter, 20 μL of MTT solution (5 mg/mL) was added and cultured for another 4 h, followed by the addition of DMSO. The cell viability was measured at the wavelength of 570 nm by Microplate Reader (ELx800, BIO-TEK Instruments Inc., USA). Dark cellular toxicity of different concentrations of ICG (5, 10, 2, and 40 μg/mL) against bEnd.3 cells was also examined. In addition, Calcein AM and EthD-III were also used to evaluate the *in vitro* cytotoxicity.

2.15. Apoptosis assay

The U87 cells were treated with the nanoparticles followed by a 3 min laser irradiation. The Annexin V-FITC apoptosis analysis was detected by flow cytometry according to the manufacturer's instructions, and processed *via* FlowJo.

2.16. Cytotoxicity of the nanoparticles in tumor spheroids

The cytotoxicity in the spheroids was detected *via* a Live/Dead Viability/Cytotoxicity Kit. The above U87 spheroids were incubated with ptHDL/siHIF-ICG, rHDL/siHIF-ICG, Lipos/siHIF-ICG, and ptHDL/siNC-ICG under laser. The spheroids were treated per manufacturer's instruction. Images were captured by CLSM and analyzed using Zen blue software.

2.17. In vivo biodistribution of nanoparticles

Animal and tumor implantation. Healthy BALB/c nude mice (18–22 g) were purchased from Shanghai Slac Laboratory Animal Co. Ltd. All procedures were approved by the China Pharmaceutical University Ethics Committee and carried out in accordance with the National Institute of Health Guide for the Care and Use of Laboratory Animals. For orthotopic glioma model, U87 cells were inoculated into the striatum (bregma right lateral 1.8 mm, back 0.6 mm, depth 3 mm). The glioma growth was monitored by *in vivo* living imaging system. RFP-U87 glioma-bearing mice were obtained by the same procedure as described above.

Nanoparticles biodistribution in glioma-bearing mice. U87 glioma-bearing mice were randomly grouped administered *via* tail injection with Lipos/Cy3-siNC-ICG, rHDL/Cy3-siNC-ICG, and ptHDL/Cy3-siNC-ICG (ICG 1.5 mg/kg), respectively. The mice were anesthetized and imaged at 6, 12, and 24 h post administration *via* Xenogen IVIS 200. For *ex vivo* fluorescence imaging, the mice were sacrificed, and major organs were collected, rinsed, and captured images. Tumor hypoxia was analyzed according to Hypoxyprobe-1 Plus Kit instructions and imaged with CLSM.

2.18. In vivo anti-glioma efficacy

Orthotopic RFP-U87 tumor cells were inoculated into BALB/c nude mice. The mice were divided into 5 groups when the tumor reached about 100 mm^3 (n = 4 in each group): (i) Saline, (ii) ptHDL/siNC-ICG (L), (iii) rHDL/siHIF-ICG (L), (iv) Lipos/siHIF-ICG (L), (v) ptHDL/siHIF-ICG (L) (siRNA: 1 mg/kg, ICG: 1.5 mg/kg). At 6 h after administration, mice in group (ii), (iii), (iv), and (v) were irradiated by laser (1 W/cm^2), denoted as (L). Meanwhile, the region maximum temperatures and infrared thermographic images of tumors were captured. The *in vivo* glioma condition after different treatments was imaged through a 3T MRI scanner at Hospital. The tumor size and body weight were recorded every other day during the experiment. The tumor long diameter (a, mm) and short diameter (b, mm) of U87 cell bearing nude mice were measured ascribed to the fluorescence of ICG, and the volume of brain tumors was calculated using the following equation:

Tumor volume (mm^3) = a × b^2/2

After infrared thermal imaging in day 17, mice were sacrificed and their brain tumor were removed under the FLI guidance of ICG, then weighed.The FLI of ICG was utilized for precise imaging-guided isolation of the tumor tissue from normal brain tissue. The tumor was resected step by step under the guidance of FLI. All the mice were sacrificed, and the tumors were collected, weighed, and used for pathological evaluation (Nissl, H&E, Ki67, Caspase-3, Bcl2, and Bax staining). The survival rate of the animals was recorded. The Western blot analysis of *in vivo* antitumor effect evaluation was the same as the mentioned above.

2.19. In vivo biosafety of ptHDL/siNC-ICG

To study the biosafety of ptHDL/siNC-ICG, healthy BALB/c mice were administrated with ptHDL/siNC-ICG through tail vein (siRNA 1 mg/kg, ICG 1.5 mg/kg). The mice injected with saline were used as control. All the mice were sacrificed at 16 d after injection, the blood samples were collected for blood biochemistry analysis, and the major organs were excised for H&E staining.

2.20. Statistical analysis

Data are presented as mean ± SD. The statistical significance was determined using one-way ANOVA followed by Tukey's post test; *$p <$ 0.05, **$p <$ 0.01, ***$p <$ 0.001.

3. Results and discussion

3.1. Preparation and characterizations of lipoprotein-biomimetic nanosystem

The nanoparticles of ptHDL/siNC-ICG were prepared by film dispersion method with encapsulated photosensitizer ICG and anchored Chol-siRNA (Fig. 2A). In order to facilitate glioma targeting and penetration of the nanoparticles in solid tumors, tLyP-1 was fused to the apolipoprotein mimetic peptide D4F. Agarose gel electrophoresis was used to investigate whether siRNA could be effectively inserted into the surface of ptHDL. As shown in Fig. S1, with the increased amount of ptHDL, the fluorescence intensity of free Chol-siRNA band in agarose gel gradually weakened. When the ratio of ptHDL and Chol-siRNA (v/v) was 4:1, the fluorescence band of siRNA stagnated completely, while no fluorescence band was visualized when the ratio was 5:1, indicating the gene was covered from overload of nanoparticles. Accordingly, the ratio between ptHDL and Chol-siRNA was determined to be 4:1.

To investigate the nanoparticle integrity and dual-drug loading, we developed a double-labeling approach where ptHDL vehicle was labeled with Cy5, and Chol-siRNA was labeled with Cy3, which were both determined by agarose gel electrophoresis. As shown in Fig. 2B, the well-merged ICG, Cy5, and Cy3 signals on lane indicated the ptHDL could stably package siRNA and ICG. The ptHDL/siNC-ICG appeared as quasi-spherical shapes with uniform nanoparticle distribution. The nanoparticles exhibited brush border after incubation with tLyP-1-fused apolipoprotein mimetic peptide, confirming the successful assembly of ptHDL/siNC-ICG (Fig. 2C). By inserting tLyP-1 to the HDL surface, the hydrodynamic diameter of the nanoparticles was increased with an average diameter of 3.5 nm (from 60.8 nm to 64.3 nm). The slight change of diameter and potential may be related to the tLyP-1surface attachment (Table S1). The encapsulation efficiency (EE%) of siRNA and ICG in rHDL/siNC-ICG and ptHDL/siNC-ICG were 80.75% of siRNA, 40.67% of ICG, and 97.65% of siRNA, 51.27% of ICG, respectively, demonstrating that the conjugation of mimetic peptides did not affect the drug loading capacity of the carriers and shape the terminal nanoparticle structure. Given that physiological stability is one of the critical prerequisites of nanoagents' biomedical applications, we examined the stability of ptHDL/siNC-ICG by monitoring the changes in particle size and zeta potential incubated in PBS (pH 7.4). As illustrated in Fig. 2D, ptHDL/siNC-ICG maintained good dimensional stability and a negative

zeta potential in the neutral medium. To confirm that the nanocarriers could protect siRNA from serum degradation and successfully deliver siRNA to the lesion region, serum stability assay has become a key indicator. Significant difference was shown in Fig. S2 to assess the ability of cholesterol conjugation and ptHDL carrier to protect siRNA from degradation in plasma. It was possible that the protein structure plays a packaging and integration role of nanoparticles. During nearly 48 h storage, the nanoparticles maintained relative structural stability, implying that ptHDL/siNC-ICG would be able to prolong the blood circulation time.

The ability of ptHDL/siNC-ICG to produce ROS was further evaluated. DCFH-DA and SOSG were used to measure the generation of ROS and $^1O_2$, respectively. A slightly less generation of ROS was detected ascribed to the compact configuration of ptHDL/siNC-ICG (Fig. 2E). No significant difference of SOSG fluorescence intensity was shown between free ICG and ptHDL/siNC-ICG group, indicating the ability of ptHDL/siNC-ICG to generate $^1O_2$ is not affected (Fig. 2E). Given that several types of ROS, including $^1O_2$, hydroxyl radicals (•OH) and superoxide anion free radical (•O_2), maybe involved during PDT process, it is crucial to identify the ROS species generated by ptHDL/siNC-ICG under NIR irradiation. Here, the ROS species were measured by an electron paramagnetic resonance spectrometer. As the signal in the electron spin resonance (ESR) spectrum indicated (Fig. 2F), a triplet ESR signal with relative intensities of 1:1:1 was captured, which is a characteristic ESR spectrum of $^1O_2$. In contrast, no obvious response was observed for ptHDL/siNC-ICG before NIR irradiation. The results manifested that ptHDL/siNC-ICG mainly produced $^1O_2$ under NIR irradiation.

To evaluate the photothermal performance of ptHDL/siNC-ICG, we investigated the photothermal profiles in different conditions, including laser power (0.2, 0.5, 0.8, 1.0, 1.2 W/cm^2), ICG concentration (5, 10, 20, 40 μg/mL), and recorded the temperature changes under laser irradiation (808 nm) within 5 min using an infrared thermal imaging camera. ptHDL/siNC-ICG displayed a temperature rise after irradiation, and the temperature was positively related to their concentration, irradiation time, and power density of the laser (Fig. 2G and H). And it showed a higher photothermal conversion efficiency (η) at a level of 51.49% than free ICG of 27.89%, pointing the superior stability of ptHDL/siNC-ICG and could efficiently convert laser energy into heat to induce local hyperthermia for photothermal therapy. The highest photothermal effect was observed in ptHDL/siHIF-ICG with a temperature elevation to 47.2 °C. The temperature of free ICG, ptHDL/siNC-ICG, Lipos/siHIF-ICG, and rHDL/siHIF-ICG increased to 40.0, 46.4, 40.1, and 43.3 °C, respectively (Fig. S3). As the stability of PTT agent is highly desirable to ensure high PTT efficacy, we determined the photothermal stability of ptHDL/siHIF-ICG upon irradiation of a laser alternatively switched on and off. There is no obvious change observed in the photothermal efficacy after five consecutive laser on/off cycles, demonstrating desirable thermostability and photostability (Fig. 2I). ICG entrapped in ptHDL and its compact structure ensured ICG stably existed, enhancing photostability of ICG. Meanwhile, the desirable photothermal efficiency also provided a prerequisite for PTT of nanoparticles *in vivo*. *In vitro* drug release from ptHDL/siNC-ICG was detected in PBS with or without laser irradiation. As shown in Fig. 2H, siRNA in Lipos/siNC-ICG released the most rapidly, and approximately 24% siRNA was free within 24 h. While the accumulative amount of siRNA release from rHDL/siNC-ICG and ptHDL/siNC-ICG were 22% and 18%, and a similar release trend was observed in the ICG release profile. Lipos/siNC-ICG group was only a bare lipid nucleus, of which the carrier structure was relatively loose, resulting in fast release profile for siRNA from Lipos. The loading pattern of siRNA in ptHDL vehicle was modified with hydrophobic cholesterol terminal embedded in phospholipid monolayer, thus ptHDL surface degradation process determined the drug release rate. Under laser irradiation, 51% of siRNA was released after the first 1 h, followed by a continuous slow-release phase. Without NIR irradiation, the core-shell structure of nanoparticles was stable, and the diffusion of siRNA and ICG was slow. Once exposed to laser irradiation, the heat generated by ICG induced whole collapse of the core-shell structure, and dramatically triggered the release of both siRNA and ICG. These results demonstrated that ptHDL/siNC-ICG could achieve on-demand drug release by laser irradiation, thereby controlling its drug-release targeting efficacy and photo-gene therapy.

3.2. In vitro cellular uptake, BBB transcytosis and tumor spheroid penetration

The efficient cellular uptake is the premise for antitumor drug delivery. Fig. 3A revealed that ptHDL/Cy3-siNC-ICG performed strong fluorescence intensity in U87 cells, indicating the effective cellular uptake. In contrast, rHDL/Cy3-siNC-ICG or Lipos/Cy3-siNC-ICG shown obviously less fluorescence, indicating that the functional lipoprotein nanoparticles constructed with fusion apolipoprotein mimetic peptides could efficiently transport cargoes to U87 cells. Quantitative analysis by flow cytometry demonstrated that ptHDL mediated siNC-ICG delivery displayed the strongest uptake behavior, and the uptake is notably reduced after pre-incubated with free tLyP-1 (Fig. 3B). The findings further confirmed the tumor-homing routine inspired by tLyP-1 modified HDL particulates would be beneficial for cargo shuttling. The feasibility of ptHDL/siNC-ICG to improve BBB permeability was further investigated. The monolayer immortalized mouse brain endothelial cells (bEnd.3) cultured was applied as *in vitro* BBB model (Fig. 3C). The *trans*-endothelial electrical resistance (TEER) values of the above bEnd.3 monolayers did not change over time, indicating the integrity of cell monolayer, and the translocation of nanoparticles was only through a transcellular pathway (Fig. S4). The transport ratio of ptHDL/Cy3-siNC-ICG were higher than that treated with rHDL/Cy3-siNC-ICG or Lipos/Cy3-siNC-ICG, demonstrating that ptHDL nanoparticles could effectively across BBB for further drug accumulation in brain (Fig. 3D & Fig. S5). It is known that tLyP-1 peptide binds tightly and specifically to NRP-1 receptor, which is expressed at high levels on the surface of cerebral microvascular endothelial cells. Thus, we hypothesized that ptHDL could deliver drugs past the BBB based on the tLyP-1 peptide-NRP-1 receptor interaction and the hypothesis was investigated in the *in vitro* BBB model. The competition experiment was conducted by pre-incubating bEnd.3 monolayer with free tLyP-1 peptide. As expected, the *in vitro* BBB transport ratio of ptHDL/Cy3-siNC-ICG was significantly decreased with free tLyP-1, demonstrating that the superior BBB permeation capacity of ptHDL/Cy3-siNC-ICG was attributed to the high affinity by NRP-1 receptors (Fig. 3D). We further verified this transport mechanism in orthotopic mice model. Such tLyP-1 pretreatment led to notable reduction of tumor accumulation of ptHDL/siNC-ICG (Fig. 3E and F).

Multicellular tumor spheroids were further prepared with U87 cells to evaluate the nanoparticle penetration. The cell-penetration capacity was observed by detecting the fluorescence of ICG and Cy3 (Fig. 3G). ptHDL mediated ICG and Cy3-siNC delivery exhibited the highest fluorescence intensity spread in most of the regions, indicating that a more extensive penetration throughout the spheroids than that of rHDL and Lipos, and facilitated a significant deep-penetration against U87 tumor spheroids. Further analysis confirmed that ptHDL/Cy3-siNC-ICG performed the deepest drug shuttling with an average penetrating depth of 65 μm in the spheroids, while rHDL group demonstrated an average penetration of 35 μm depth. The double positive cell rate in ptHDL group by flow cytometry analysis was up to 80.76%, demonstrating a significant increase compared with other control groups (39.4% of Lipos, 61.25% of rHDL). The improved tumor-targeted penetration capacity of ptHDL/Cy3-siNC-ICG is a result of tLyP-1 fusion, which increased nanoparticle cellular uptake, and enhanced drug shuttling into tumors. Above all, we demonstrated that the functional lipoprotein nanoparticles prepared with tLyP-1-fused apolipoprotein mimetic peptides could enhance the drugs to site-specific accumulation in tumor.
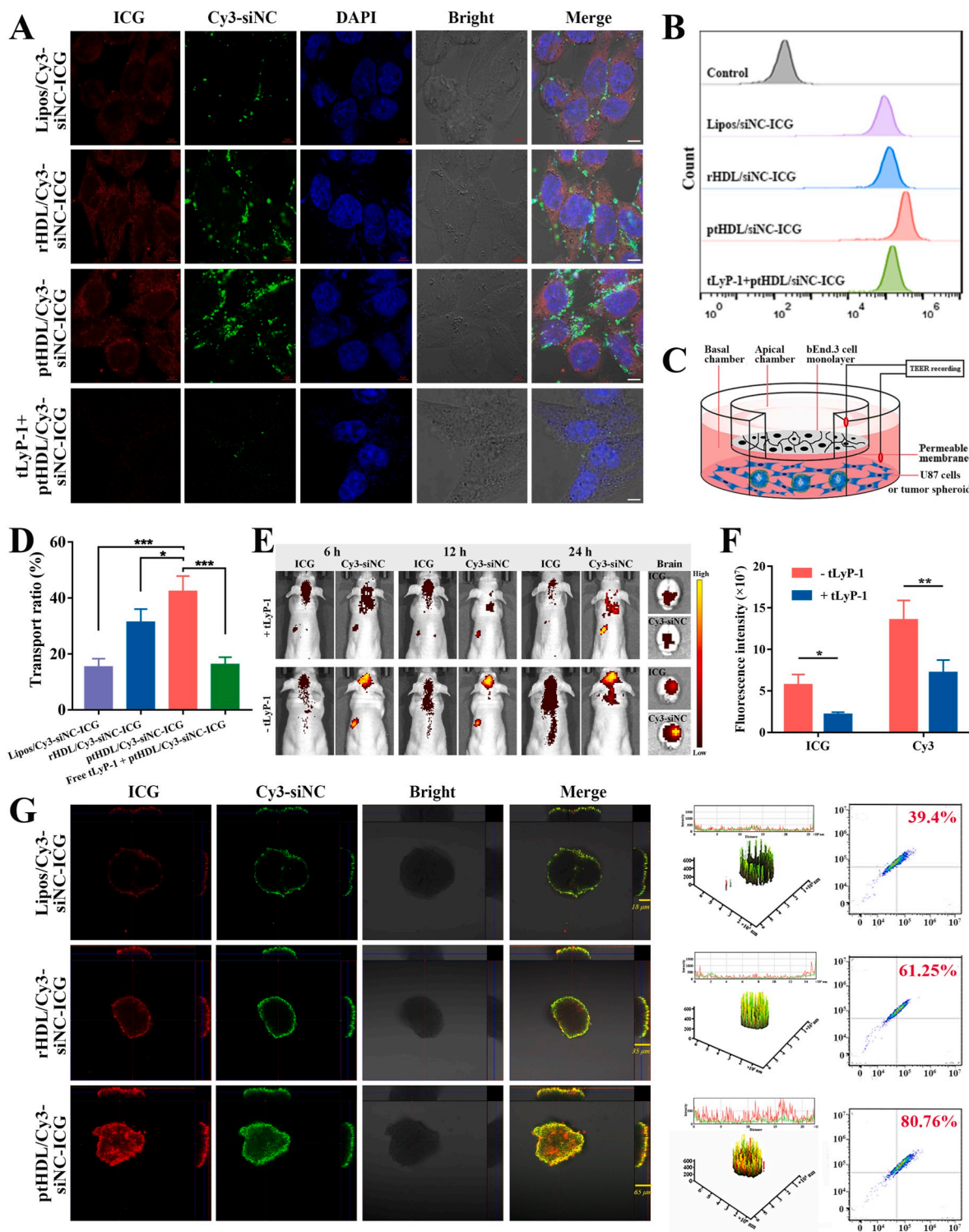
Fig. 3. *In vitro* cellular uptake, BBB transcytosis and tumor spheroid penetration. (A) Cellular uptake of different nanoparticles on U87 cells in the presence of BBB model *in vitro*. Scale bar: 5 μm. (B) For flow cytometry analysis for cellular uptake of various preparations by U87 cells after 4 h. (C) Schematic illustration of the *in vitro* BBB model. (D) The transport ratio (%) of nanoparticles across the BBB *in vitro*. (E) Qualitative and (F) semi-quantitative analysis of the tumor accumulation of ptHDL/Cy3-siNC-ICG at 6 h, 12 h, and 12 h post-injection in the mice bearing intracranial U87 glioma after the pretreatment with tLyP-1 or vehicle only. (G) The nanoparticles penetrated in U87 spheroids. CLSM images of spheroids treated with Lipos/Cy3-siNC-ICG, rHDL/Cy3-siNC-ICG, ptHDL/Cy3-siNC-ICG (*x*, *y* and *z* directions). Surface plot images of spheroids with different treatments. Accumulation of ICG and Cy3-siNC in U87 cells from spheroids were analyzed by flow cytometry.
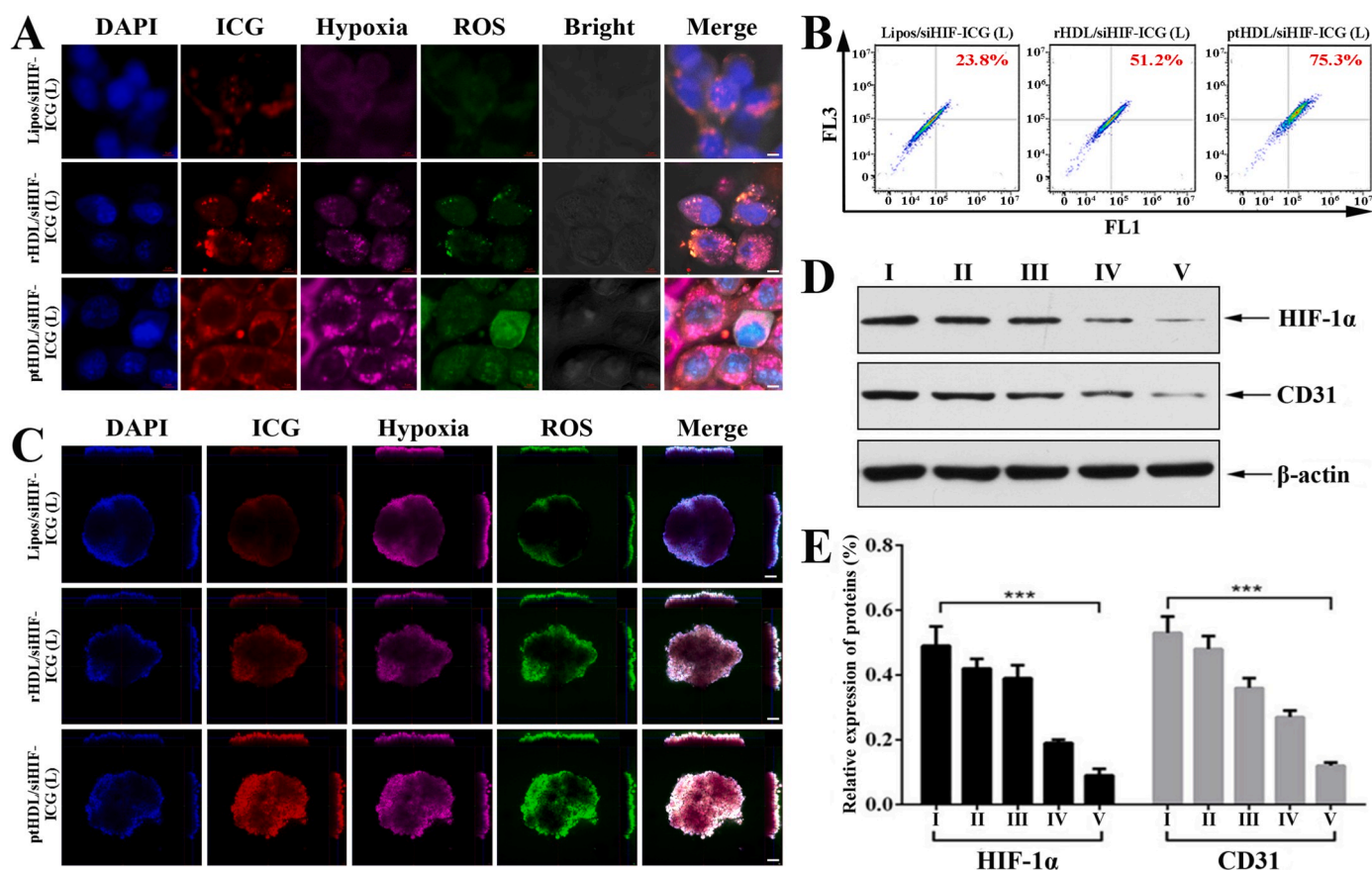
3.3. Cellular microenvironment studies

The conversion of oxygen to ROS through the action of ICG would generate hypoxic status in TME. In such hypoxic state, the delivery of siHIF would silence the over-expression of HIF-1α, contributed to the selective killing of hypoxic tumor cells. To confirm nanoparticle-mediated ROS generation and hypoxia in the tumor cells, U87 cells were incubated with different preparations and analyzed under laser. The fluorescence intensity was positively correlated with the ROS and hypoxia generation intracellularly. In comparison with rHDL/siHIF-ICG and Lipos/siHIF-ICG, U87 cells treated with ptHDL/siHIF-ICG plus laser induced intense fluorescence, demonstrating that ptHDL group induced greatly increased ROS levels and more pronounced hypoxia (Fig. 4A and B). The enhanced cellular uptake of ptHDL/siHIF-ICG probably account for higher ROS production, and subsequent hypoxia generation in TME. The results indicated that ptHDL/siHIF-ICG treatment produced more ROS and subsequent intracellular hypoxia generation, which was well-established for siHIF playing an interference role. Afterwards, the ROS generation and hypoxia production were investigated in tumor spheroids. The inner and peri-necrotic rim of U87 spheroids was hypoxic, consistent with ROS generation regions (Fig. 4C). The ptHDL group facilitated a more extensive ICG distribution in such regions than that of rHDL or Lipos, further confirming ptHDL provided high PDT efficacy in 3D tumor model. As reported, the upregulation of HIF-1α and the related downstream gene such as VEGF, were triggered adapting to the hypoxic environment during tumor growth. HIF-1α is related to hypoxia tolerance of tumor cells, and the overexpression could promote tumor growth. CD31 is a transmembrane glycoprotein over-expressed in endothelial cells, and considered as a reliable marker of angiogenesis in various tumor blood vessels [43]. Notably, the obviously decreased expression level of HIF-1α and CD31 proteins was detected in ptHDL/siHIF-ICG-incubated U87 cells (Fig. 4D). And significant differences were shown between ptHDL/siHIF-ICG (L) and other groups (Fig. 4E). It was verified that HIF-1α and CD31 proteins were highly expressed under hypoxia tension and downregulated after ptHDL/siHIF-ICG (L) treatment, which may contribute to hypoxic tumor cells death.

3.4. In vitro cytotoxicity on tumor cells and spheroids

In vitro photo-gene therapeutic performance of the designed nanoplatform was quantitatively assessed by a standard MTT assay. The combinational photo-gene therapy mediated by ptHDL/siHIF-ICG were measured in U87 cells. The ptHDL/siNC-ICG with laser irradiation treatment resulted in a 61.33% inhibition of cell viability, suggesting the significant inhibitory effects of phototherapy alone. Of note, the ptHDL/siHIF-ICG (L) caused a 95.70% inhibition of cell viability, which was more effective than Lipos and rHDL-mediated photo-gene therapy (Fig. S6). In addition, dose dependent cytotoxicity of the ptHDL/siNC-ICG composite against bEnd.3 cells was evaluated under dark conditions, and the results indicated negligible dark cytotoxicity (Fig. S7). The U87 cell viability after exposure to various formulations were also evaluated by using a Live/Dead Viability/Cytotoxicity kit. As shown in Fig. 5A, ptHDL/siHIF-ICG group contributed to a large amount of dead cells, while control groups showed widely distributed live cells. The results confirmed that ptHDL/siHIF-ICG performed the superior

Fig. 4. Cellular microenvironment studies. (A) ROS and hypoxia generation in the cells with nanoparticles under laser. CLSM images of the cells stained with ROS and hypoxia probes in the presence of BBB model *in vitro*. Scale bar: 5 μm. (B) ROS and hypoxia generation analyzed by flow cytometry. (C) ROS and hypoxia generation in the tumor spheroids. Scale bar: 50 μm. (D) Representative immunoblots of HIF-1α and CD31 protein expression in U87 cells transfection assayed by Western blot. I: Control; II: ptHDL/siNC-ICG (L); III: Lipos/siHIF-ICG (L); IV: rHDL/siHIF-ICG (L); V: ptHDL/siHIF-ICG (L). (E) Quantitative analysis from Western blot were indicated as mean ± SD (n = 3). ***$p < 0.001$, compared with control group. (L) stands for "laser".
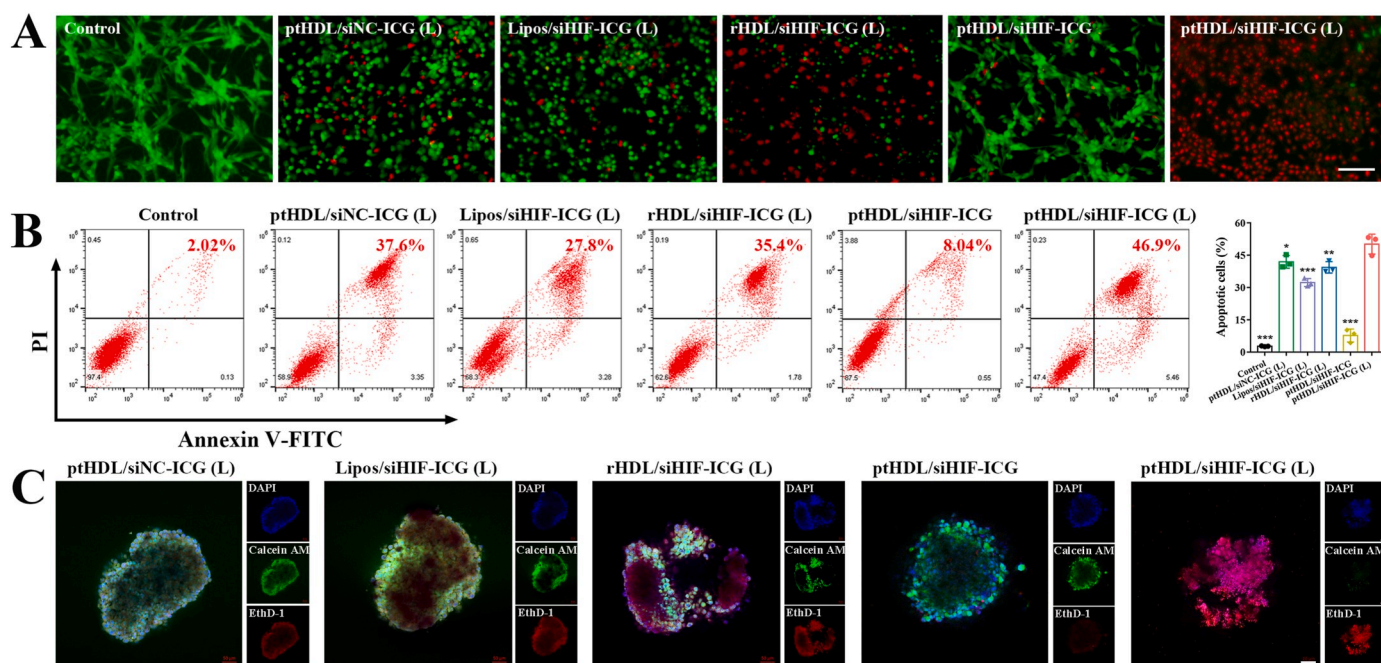
Fig. 5. *In vitro* cytotoxicity on tumor cells and spheroids. (A) The live/dead viability assays in U87 cells. Scale bar: 100 μm. (B) Flow cytometry assay and quantitative analysis of apoptosis induced on U87 cells by various nanoparticles with the same siRNA concentration of 100 nM. (C) The live/dead viability assays in U87 tumor spheroids. Live cells were labeled with calcein AM (green), and the dead cells were stained with EthD-1 (red). Nucleus was stained with DAPI (blue). Scale bar: 50 μm.

cytotoxicity to tumor cells among various formulations. Moreover, the percentage of apoptotic cells in ptHDL/siHIF-ICG (L) was 50.20%, significantly higher than that of Lipos/siHIF-ICG (32.33%), rHDL/siHIF-ICG (39.37%), and ptHDL/siNC-ICG (41.96%), respectively (Fig. 5B). The enhanced tumor cell killing effect could be resulted from the higher intracellular uptake. The results demonstrated that ptHDL enabled efficient synergistic therapy, thereby enhancing antitumor therapeutic efficacy. The cell killing efficacy of ptHDL/siHIF-ICG on the spheroids was also evaluated by live/dead assay (Fig. 5C). The control untreated spheroids showed intact morphology, compact structure, and only a limited number of dead cells, indicating no obvious antitumor efficacy. In contrast, the treatment with ptHDL/siHIF-ICG (L) contributed to the broken tumor spheroid structure, and a large amount of dead cells in spheroids. These results confirmed that ptHDL combined with laser irradiation possessed the significant cell killing efficacy. These above results clearly demonstrated that tLyP-1-fused nanoparticles could not only improve tumor penetration, but also promote cell death within the 3D tumor spheroids environment.

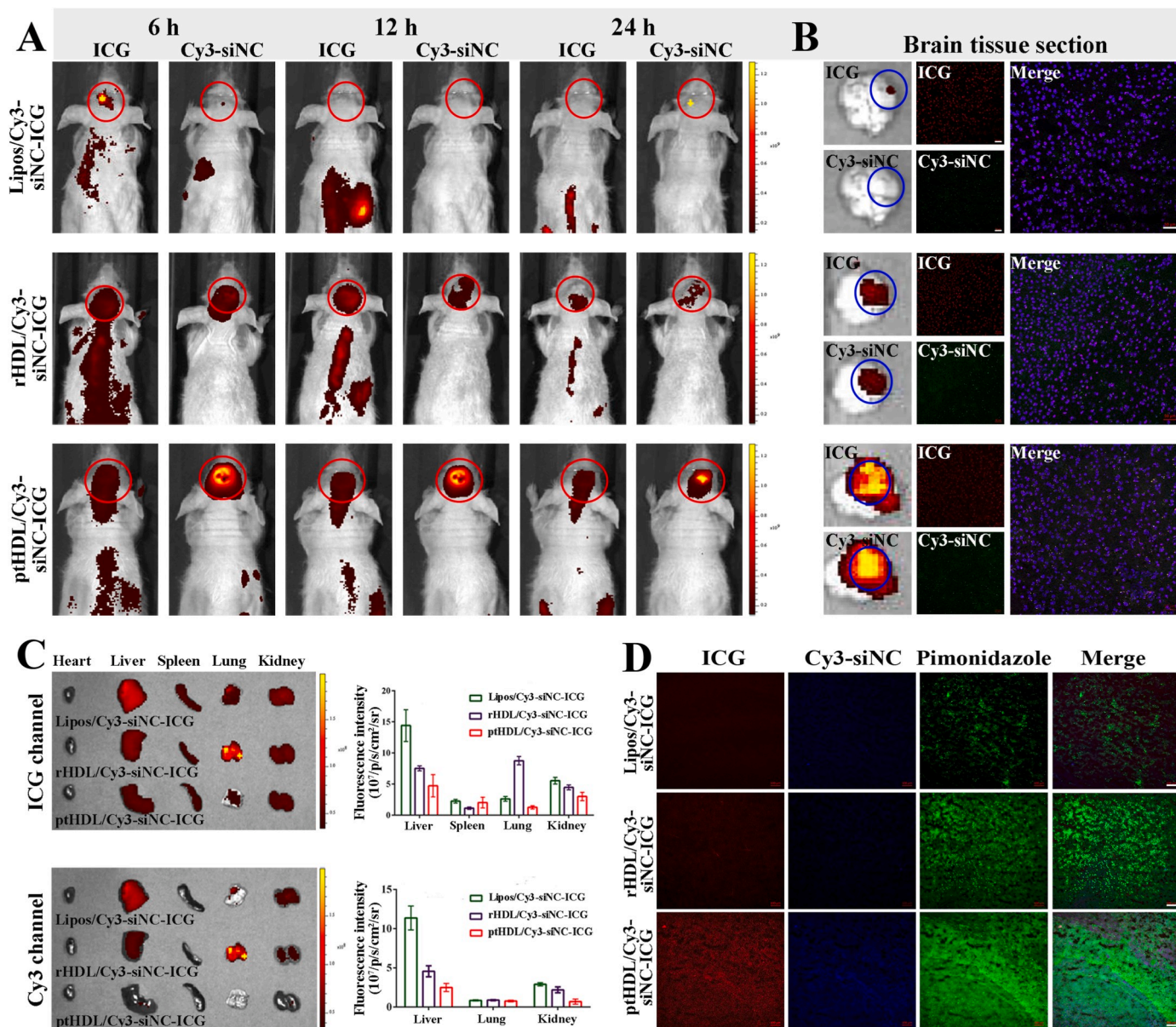### 3.5. In vivo biodistribution of nanoparticles

The whole-body fluorescence images of orthotopic U87 tumor-bearing nude mice were performed at 6, 12, and 24 h after intravenous administration. As exhibited in Fig. 6A, the brain of the mice showed intense fluorescence after 6 h, indicating a substantial ptHDL accumulation in brain. Moreover, a strong fluorescence localized in the tumor regions at 24 h after treated with ptHDL/Cy3-siNC-ICG was still observed, which was beneficial from the long-circulation of ptHDL. In contrast, comparatively less fluorescence was found in the brain of rHDL group. The brain drug accumulation decreased over time, and most of fluorescence in brain disappeared after 24 h post-injection. However, there was hardly fluorescence signal observed in Lipos/Cy3-siNC-ICG. The *ex vivo* fluorescence images further demonstrated that ptHDL nanoparticles could selectively accumulate in tumor site rather than distributed throughout the brain, indicating an efficient tumor-homing capacity of the nanoparticles (Fig. 6B). The major organs were then collected, of which the fluorescence signal was further investigated for

lesion-drug concentration detection. As shown in Fig. 6C, the fluorescence intensity in other main organs was significantly weaker in ptHDL/Cy3-siNC-ICG-treated mice than the control groups, indicating that most of ptHDL nanoparticles accumulated in the tumor site. Collectively, ptHDL vehicle could carry Chol-siRNA and ICG to accumulate in glioma. To further evaluate the tumor hypoxia state caused by ptHDL/Cy3-siNC-ICG (L), the frozen tumor tissue sections of each group were examined by using pimonidazole. Pimonidazole is a well-characterized hypoxic marker, which forms protein adducts under hypoxic conditions and could be visualized by immunohistochemical staining. As shown in Fig. 6D, the fluorescence signal of ptHDL/Cy3-siNC-ICG displayed an extensive distribution throughout the tumor tissue, and to a significant extent overlapped with the hypoxic areas. The above results confirmed the existence of hypoxic conditions inside TME in U87 orthotopic tumor-bearing mice, and indicated the ability of ptHDL/Cy3-siNC-ICG to reach the hypoxic regions.

3.6. In vivo anti-glioma activity

Given the previous finding of the superior tumor penetration and tumor-targeting capability, we confirmed that ptHDL/siHIF-ICG could be transported into tumor cells, generating ROS under laser irradiation, thereby specifically silencing HIF-1α gene TME, which provided a combined efficient anti-glioma efficacy. The orthotopic U87 tumor-bearing nude mice were randomly divided into the following 5 groups, including saline, ptHDL/siNC-ICG (L), Lipos/siHIF-ICG (L), rHDL/siHIF-ICG (L), and ptHDL/siHIF-ICG (L) (Fig. 7A). The tumor size of the intracranial glioma was monitored by fluorescence using the IVIS imaging system. As demonstrated in Fig. 7B, the ptHDL/siHIF-ICG group gave clearly weaker fluorescence intensity and a smaller area than other groups, indicating the shrinking tumors. The ptHDL/siHIF-ICG (L) significantly inhibited tumor growth, of which the inhibitory rate was 87.21% (Fig. 7C&D). The median survival time of mice in ptHDL/siHIF-ICG (L) group was significantly longer than those in control groups (Fig. 7E). The highest anti-glioma efficiency and the prolonged survival period achieved by ptHDL/siHIF-ICG (L) were attributed to enhanced tumor-targeted penetration by tLyP-1 fusion and codelivery of gene drug

Fig. 6. *In vivo* biodistribution of nanoparticles. (A) *In vivo* images of intracranial U87 glioma bearing mice after treated with different formulations. (B) *Ex vivo* images of the brains of intracranial U87 glioma bearing mice. CLSM images of glioma sections from U87 bearing BALB/c mice. Nuclei were stained with DAPI (blue), ICG was in red, and Cy3-siNC was in green. Scale bar: 50 μm. (C) Quantification of *ex vivo* tumor fluorescence intensity (Data are presented as mean ± SD, n = 3). (D) Hypoxia visualization in U87 tumors. The frozen tumor sections labeled with the pimonidazole antibody (green), ICG was in red, and Cy3-siNC was in blue. Scale bar: 100 μm.

and photosensitizer.

3.7. In vivo potential mechanisms for synergistic photo-gene therapy

As shown in T1-weighted MRI images, the size of glioma region was smaller and the depth was shallower than all other groups, indicating a lighter glioma (Fig. 8A). Analysis of the Nissl and H&E tumor sections indicated large area shadow in the saline group, while no visible tissue damage is observed in the brain of ptHDL/siHIF-ICG group (Fig. 8B). While, tumor cells in the ptHDL/siHIF-ICG treated group exhibited a decrease of Ki-67 and Bcl2 expression, and increase of Caspase-3 expression, revealed significant apoptosis and antitumor effect of our nanoparticles (Fig. 8C and D). Encouraged by the superior photothermal efficacy of ptHDL/siHIF-ICG *in vitro*, the *in vivo* PTT evaluation of glioma bearing mice was further investigated (Fig. 8E). The central temperature of tumors in ptHDL/siHIF-ICG group reached 46.7 °C, while that of free saline group just rose to 39.9 °C. For comparison, the Lipos and rHDL

groups contributed to an increasing temperature to 43.7 and 44.3 °C (Fig. 8F). Our results indicated that ptHDL/siHIF-ICG achieved the highest PTT efficiency, most likely due to the enhanced targetability and photostability of ICG in ptHDL carrier. We further evaluated the expression of relevant proteins by Western blot, demonstrating the reduced HIF-1α and CD31 expression levels after ptHDL/siHIF-ICG (L) treatment in the orthotopic glioma (Fig. 8G). It also showed that the expression level in ptHDL/siHIF-ICG (L) group was significantly different from that in other groups (Fig. 8H). The remarkably decreased HIF-1α expression level contributed to the inhibition of tumor angiogenesis and induction of tumor cell apoptosis. Furthermore, as a recognized marker of angiogenesis, CD31 expression was thus downregulated.

The biosafety of ptHDL/siNC-ICG was then investigated. In the orthotopic glioma model, no obvious difference in body weight was found in the mice from each group, suggesting the low toxicity of the nanoparticles *in vivo* (Fig. S7). After the treatment, we also performed
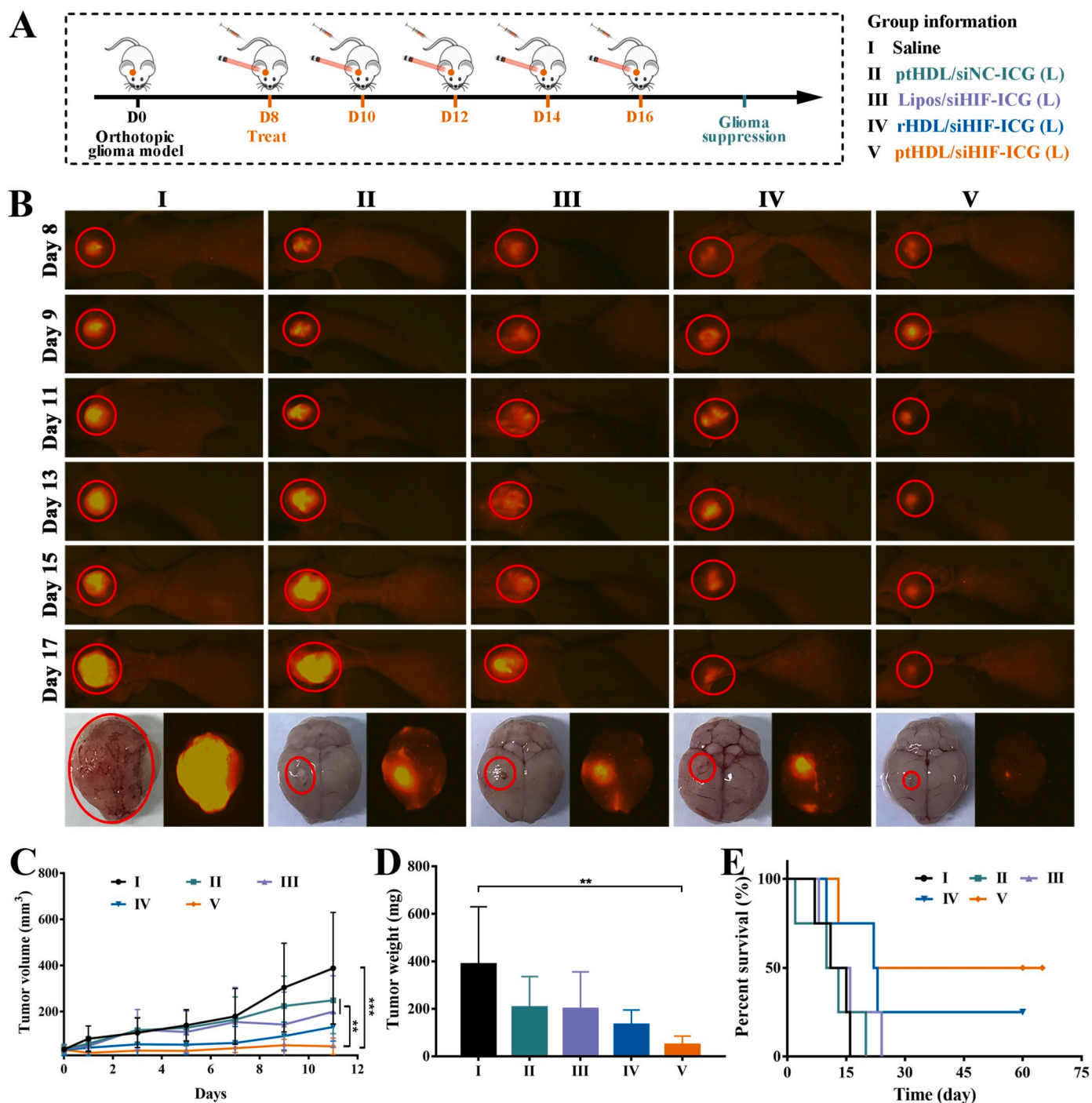
Fig. 7. *In vivo* anti-glioma activity of ptHDL/siHIF-ICG. (A) *In vivo* experimental protocol for the delivery of ptHDL/siHIF-ICG in U87 glioma mouse tumor model. (B) The changes of fluorescence in brain glioma treated with different formulations. (C) Tumor growth profiles in mice treated with various formulations. (D) Tumor weight inhibition. (E) The survival curves. Data are presented as mean ± SD; **$p < 0.01$, ***$p < 0.001$. (L) stands for "laser".

blood routine and pathologic examinations through hemanalysis and H&E staining. The hemanalysis data indicated no significant changes in the numbers of peripheral blood cells as well as liver and kidney functions after injection of ptHDL/siNC-ICG (Fig. S8). The H&E staining of tissue sections exhibited that there was no obvious damage to major organs in ptHDL/siNC-ICG group, when compared to the untreated group, confirmed the desirable biocompatibility from bionic design (Fig. S9).

4. Conclusions

In this study, we presented a lipoprotein-biomimetic nanoparticle of ptHDL/siHIF-ICG, which mimicked the natural structure and function of HDL nanoparticles, and simultaneously delivered ICG and siHIF to solid tumor deep regions for combined therapy of PDT, PTT and siRNA gene silencing against glioma. Inspired from lipoprotein mimic structure, ptHDL vehicle was provided with high affinity to the lipoprotein receptors on the surface of brain endothelial cells, and promoted BBB crossing. The fusion of tLyP-1 and D4F could further enhance the tumor-targeted penetration for nanoparticle accumulation in lesion. Newly
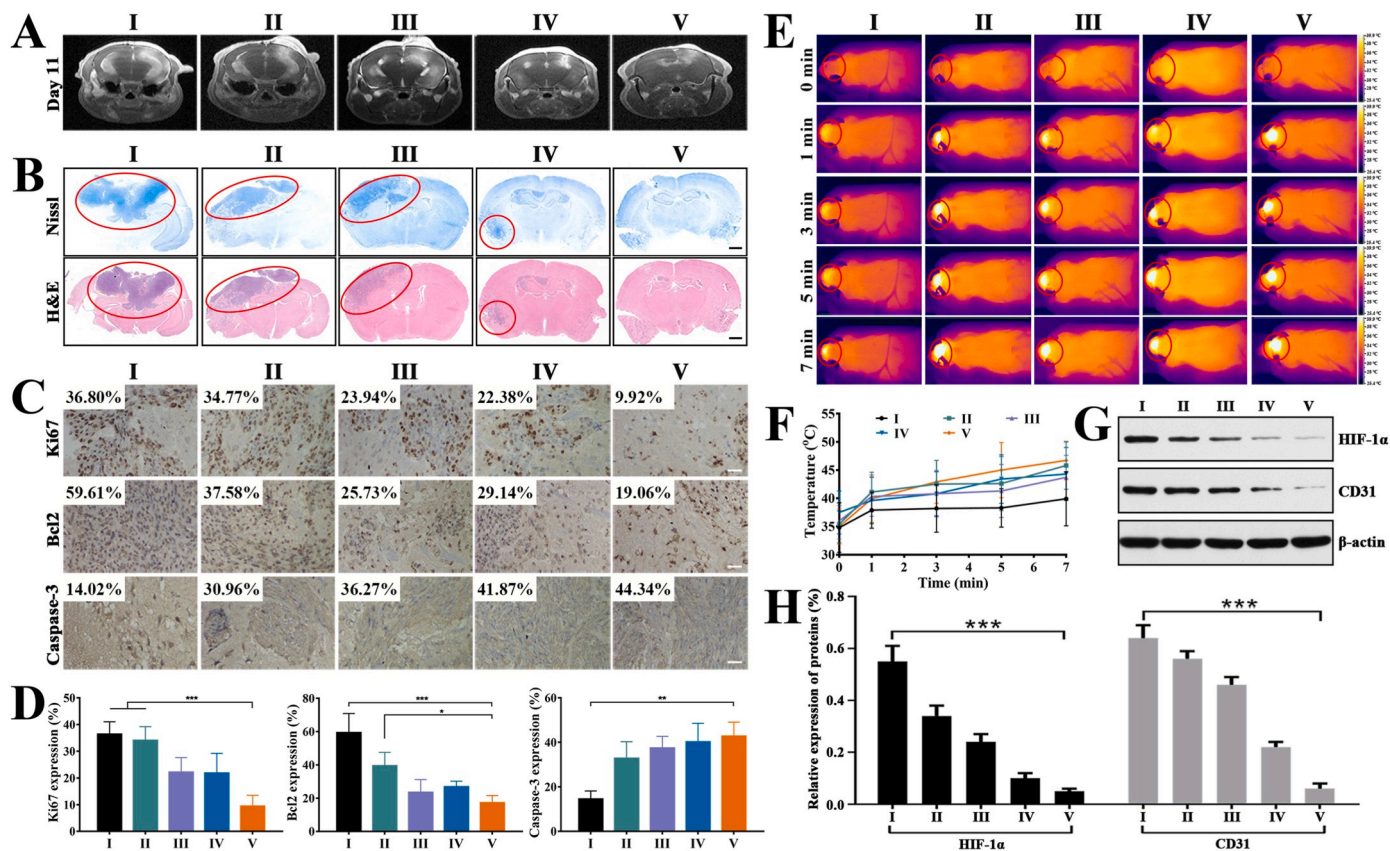
Fig. 8. (A) MRI images of brains in tumor-bearing mice treated with different formulations. (B) Nissl, H&E staining of brain glioma tissues. Scale bar: 1 mm. (C) Ki67, Bcl2, and Caspase-3 staining of brain glioma tissues. Scale bar: 50 μm. (D) Quantitative analysis from Ki67, Bcl2 and Caspase-3 staining were expressed as mean ± SD (n = 3). ***$p < 0.001$, compared with control group. (E) IR thermal images of tumor-bearing mice. (F) Temperature changes on tumor sites according to the imaging of (D). (G) Representative immunoblots of HIF-1α and CD31 protein expression in U87 cells *in vivo* at day 12 after *i.v.* treatment assayed by Western blot. I: Saline; II: ptHDL/siNC-ICG (L); III: Lipos/siHIF-ICG (L); IV: rHDL/siHIF-ICG (L); V: ptHDL/siHIF-ICG (L). (H) Quantitative analysis from Western blot were expressed as mean ± SD (n = 3). ***$p < 0.001$, compared with control group. (L) stands for "laser".

established ptHDL/siHIF-ICG not only exhibited effective $^1O_2$ generation capability under NIR laser irradiation, but also achieved nondestructive monitoring and diagnosis of glioma *in situ* depending on the real-time targeted NIR fluorescence of ICG. Owing to the ROS and hyperthermia generated from ICG, the gene of siHIF was burst released from the nanoparticles and transported into the tumor cell target mRNA–HIF–1α, resulting in high efficacy of gene silencing. The designed lipoprotein-biomimetic nanoparticles could maximize the synergistic effect of various theranostics, and provide a potent strategy for precise tumor localization and early diagnosis, targeting, long-acting and combined therapy of glioma.

CRediT authorship contribution statement

Ruoning Wang: Conceptualization, Investigation, Validation, Data curation, Formal analysis, Software, Writing – original draft. **Xiaohong Wang:** Validation, Visualization, Formal analysis. **Junsong Li:** Validation, Visualization. **Liuqing Di:** Writing – review & editing. **Jianping Zhou:** Conceptualization, Resources, Writing – review & editing, Project administration. **Yang Ding:** Conceptualization, Supervision, Resources, Writing – review & editing, Project administration.

Declaration of competing interest

The authors declare that they have no known competing financial interests or personal relationships that could have appeared to influence the work reported in this paper.

Acknowledgments

Appendix A. Supplementary data

Supplementary data to this article can be found online at https://doi.org/10.1016/j.bioactmat.2021.10.039.

References

[1] Q.T. Ostrom, H. Gittleman, G. Truitt, A. Boscia, C. Kruchko, J.S. Barnholtz-Sloan, CBTRUS statistical report: primary brain and other central nervous system tumors diagnosed in the United States in 2011-2015, Neuro Oncol. 20 (suppl_4) (2018) iv1–iv86.

[2] A.C. Tan, D.M. Ashley, G.Y. López, M. Malinzak, H.S. Friedman, M. Khasraw, Management of glioblastoma: state of the art and future directions, CA Cancer J. Clin. 70 (4) (2020) 299–312.

[3] R. Pandit, L. Chen, J. Götz, The blood-brain barrier: physiology and strategies for drug delivery, Adv. Drug Deliv. Rev. 165–166 (2020) 1–14.

[4] Z. Zhao, A.R. Nelson, C. Betsholtz, B.V. Zlokovic, Establishment and dysfunction of the blood-brain barrier, Cell 163 (5) (2015) 1064–1078.

[5] C.D. Arvanitis, G.B. Ferraro, R.K. Jain, The blood-brain barrier and blood-tumour barrier in brain tumours and metastases, Nat. Rev. Cancer 20 (1) (2020) 26–41.

[6] J.N. Sarkaria, L.S. Hu, I.F. Parney, D.H. Pafundi, D.H. Brinkmann, N.N. Laack, C. Giannini, T.C. Burns, S.H. Kizilbash, J.K. Laramy, K.R. Swanson, T.J. Kaufmann, P.D. Brown, N.Y.R. Agar, E. Galanis, J.C. Buckner, W.F. Elmquist, Is the blood-brain barrier really disrupted in all glioblastomas? A critical assessment of existing clinical data, Neuro Oncol. 20 (2) (2018) 184–191.

[7] Y. Wu, Q. Fan, F. Zeng, J. Zhu, J. Chen, D. Fan, X. Li, W. Duan, Q. Guo, Z. Cao, K. Briley-Saebo, C. Li, X. Tao, Peptide-functionalized nanoinhibitor restrains brain tumor growth by abrogating mesenchymal-epithelial transition factor (MET) signaling, Nano Lett. 18 (9) (2018) 5488–5498.

[8] Y. Liu, P. Bhattarai, Z. Dai, X. Chen, Photothermal therapy and photoacoustic imaging *via* nanotheranostics in fighting cancer, Chem. Soc. Rev. 48 (7) (2019) 2053–2108.

[9] S.S. Lucky, K.C. Soo, Y. Zhang, Nanoparticles in photodynamic therapy, Chem. Rev. 115 (4) (2015) 1990–2042.

[10] J. Chen, T. Fan, Z. Xie, Q. Zeng, P. Xue, T. Zheng, Y. Chen, X. Luo, H. Zhang, Advances in nanomaterials for photodynamic therapy applications: status and challenges, Biomaterials 237 (2020), 119827.

[11] X. Tan, S. Luo, L. Long, Y. Wang, D. Wang, S. Fang, Q. Ouyang, Y. Su, T. Cheng, C. Shi, Structure-guided design and synthesis of a mitochondria-targeting near-infrared fluorophore with multimodal therapeutic activities, Adv. Mater. 29 (43) (2017).

[12] J. Wang, J. Sun, W. Hu, Y. Wang, T. Chou, B. Zhang, Q. Zhang, L. Ren, H. Wang, A Porous Au@Rh bimetallic core-shell nanostructure as an H_2O_2-driven oxygenerator to alleviate tumor hypoxia for simultaneous bimodal imaging and enhanced photodynamic therapy, Adv. Mater. 32 (22) (2020), e2001862.

[13] C. Liu, Y. Cao, Y. Cheng, D. Wang, T. Xu, L. Su, X. Zhang, H. Dong, An open source and reduce expenditure ROS generation strategy for chemodynamic/photodynamic synergistic therapy, Nat. Commun. 11 (1) (2020) 1735.

[14] W.L. Liu, T. Liu, M.Z. Zou, W.Y. Yu, C.X. Li, Z.Y. He, M.K. Zhang, M.D. Liu, Z.H. Li, J. Feng, X.Z. Zhang, Aggressive man-made red blood cells for hypoxia-resistant photodynamic therapy, Adv. Mater. 30 (35) (2018), e1802006.

[15] X. Yang, Y. Yang, F. Gao, J.J. Wei, C.G. Qian, M.J. Sun, Biomimetic hybrid nanozymes with self-supplied H^+ and accelerated O_2 generation for enhanced starvation and photodynamic therapy against hypoxic tumors, Nano Lett. 19 (7) (2019) 4334–4342.

[16] W.R. Wilson, M.P. Hay, Targeting hypoxia in cancer therapy, Nat. Rev. Cancer 11 (6) (2011) 393–410.

[17] J.M. Brown, W.R. Wilson, Exploiting tumour hypoxia in cancer treatment, Nat. Rev. Cancer 4 (6) (2004) 437–447.

[18] A.L. Harris, Hypoxia-a key regulatory factor in tumour growth, Nat. Rev. Cancer 2 (1) (2002) 38–47.

[19] W.G. Kaelin, P.J. Ratcliffe, Oxygen sensing by metazoans: the central role of the HIF hydroxylase pathway, Mol. Cell 30 (4) (2008) 393–402.

[20] G.L. Semenza, Hypoxia-inducible factors: mediators of cancer progression and targets for cancer therapy, Trends Pharmacol. Sci. 33 (4) (2012) 207–214.

[21] P. Prasad, C.R. Gordijo, A.Z. Abbasi, A. Maeda, A. Ip, A.M. Rauth, R.S. DaCosta, X. Y. Wu, Multifunctional albumin-MnO_2 nanoparticles modulate solid tumor microenvironment by attenuating hypoxia, acidosis, vascular endothelial growth factor and enhance radiation response, ACS Nano 8 (4) (2014) 3202–3212.

[22] Y. Zou, X. Sun, Y. Wang, C. Yan, Y. Liu, J. Li, D. Zhang, M. Zheng, R.S. Chung, B. Shi, Single siRNA nanocapsules for effective siRNA brain delivery and glioblastoma treatment, Adv. Mater. 32 (24) (2020), e2000416.

[23] J. Kokkinos, R.M.C. Ignacio, G. Sharbeen, C. Boyer, E. Gonzales-Aloy, D. Goldstein, A. Australian Pancreatic Cancer Genome Initiative, J.A. McCarroll, P.A. Phillips, Targeting the undruggable in pancreatic cancer using nano-based gene silencing drugs, Biomaterials 240 (2020), 119742.

[24] B. Kim, J.H. Park, M.J. Sailor, Rekindling RNAi therapy: materials design requirements for in vivo siRNA delivery, Adv. Mater. 31 (49) (2019), e1903637.

[25] W. Viricel, A. Mbarek, J. Leblond, Switchable lipids: conformational change for fast pH-triggered cytoplasmic delivery, Angew. Chem. Int. Ed Engl. 54 (43) (2015) 12743–12747.

[26] O.F. Khan, P.S. Kowalski, J.C. Doloff, J.K. Tsosie, V. Bakthavatchalu, C.B. Winn, J. Haupt, M. Jamiel, R. Langer, D.G. Anderson, Endothelial siRNA delivery in nonhuman primates ysing ionizable low-molecular weight polymeric nanoparticles, Sci. Adv. 4 (6) (2018), eaar8409.

[27] J.M. Priegue, D.N. Crisan, J. Martínez-Costas, J.R. Granja, F. Fernandez-Trillo, J. Montenegro, In situ functionalized polymers for siRNA delivery, Angew. Chem. Int. Ed Engl. 55 (26) (2016) 7492–7495.

[28] A. Kohata, P.K. Hashim, K. Okuro, T. Aida, Transferrin-appended nanocaplet for transcellular siRNA delivery into deep tissues, J. Am. Chem. Soc. 141 (7) (2019) 2862–2866.

[29] D.H. Park, J. Cho, O.J. Kwon, C.O. Yun, J.H. Choy, Biodegradable inorganic nanovector: passive versus active tumor targeting in siRNA transportation, Angew. Chem. Int. Ed. Engl. 55 (14) (2016) 4582–4586.

[30] X. Xu, J. Wu, Y. Liu, P.E. Saw, W. Tao, M. Yu, H. Zope, M. Si, A. Victorious, J. Rasmussen, D. Ayyash, O.C. Farokhzad, J. Shi, Multifunctional envelope-type siRNA delivery nanoparticle platform for prostate cancer therapy, ACS Nano 11 (3) (2017) 2618–2627.

[31] Z. Chai, D. Ran, L. Lu, C. Zhan, H. Ruan, X. Hu, C. Xie, K. Jiang, J. Li, J. Zhou, J. Wang, Y. Zhang, R.H. Fang, L. Zhang, W. Lu, Ligand-modified cell membrane enables the targeted delivery of drug nanocrystals to glioma, ACS Nano 13 (5) (2019) 5591–5601.

[32] Y. Liu, Y. Zou, C. Feng, A. Lee, J. Yin, R. Chung, J.B. Park, H. Rizos, W. Tao, M. Zheng, O.C. Farokhzad, B. Shi, Charge conversional biomimetic nanocomplexes as a multifunctional platform for boosting orthotopic glioblastoma RNAi therapy, Nano Lett. 20 (3) (2020) 1637–1646.

[33] Q. Zhu, X. Ling, Y. Yang, J. Zhang, Q. Li, X. Niu, G. Hu, B. Chen, H. Li, Y. Wang, Z. Deng, Embryonic stem cells-derived exosomes endowed with targeting properties as chemotherapeutics delivery vehicles for glioblastoma therapy, Adv. Sci. 6 (6) (2019), 1801899.

[34] G. Jia, Y. Han, Y. An, Y. Ding, C. He, X. Wang, Q. Tang, NRP-1 targeted and cargo-loaded exosomes facilitate simultaneous imaging and therapy of glioma in vitro and in vivo, Biomaterials 178 (2018) 302–316.

[35] S. Busatto, S.A. Walker, W. Grayson, A. Pham, M. Tian, N. Nesto, J. Barklund, J. Wolfram, Lipoprotein-based drug delivery, Adv. Drug Deliv. Rev. 159 (2020) 377–390.

[36] W.J.M. Mulder, M.M.T. van Leent, M. Lameijer, E.A. Fisher, Z.A. Fayad, C. Pérez-Medina, High-density lipoprotein nanobiologics for precision medicine, Acc. Chem. Res. 51 (1) (2018) 127–137.

[37] R. Wang, C. Zhang, J. Li, J. Huang, Y. Opoku-Damoah, B. Sun, J. Zhou, L. Di, Y. Ding, Laser-triggered polymeric lipoproteins for precision tumor penetrating theranostics, Biomaterials 221 (2019), 119413.

[38] L. Roth, L. Agemy, V.R. Kotamraju, G. Braun, T. Teesalu, K.N. Sugahara, J. Hamzah, E. Ruoslahti, Transtumoral targeting enabled by a novel neuropilin-binding peptide, Oncogene 31 (33) (2012) 3754–3763.

[39] L. Zhu, H. Zhao, Z. Zhou, Y. Xia, Z. Wang, H. Ran, P. Li, J. Ren, Peptide-functionalized phase-transformation nanoparticles for low intensity focused ultrasound-assisted tumor imaging and therapy, Nano Lett. 18 (3) (2018) 1831–1841.

[40] Q. Lei, S.B. Wang, J.J. Hu, Y.X. Lin, C.H. Zhu, L. Rong, X.Z. Zhang, Stimuli-responsive "cluster bomb" for programmed tumor therapy, ACS Nano 11 (7) (2017) 7201–7214.

[41] H.B. Pang, G.B. Braun, T. Friman, P. Aza-Blanc, M.E. Ruidiaz, K.N. Sugahara, T. Teesalu, E. Ruoslahti, An endocytosis pathway initiated through neuropilin-1 and regulated by nutrient availability, Nat. Commun. 5 (2014) 4904.

[42] C. Liu, S. Zhang, J. Li, J. Wei, K. Müllen, M. Yin, A water-soluble, NIR-absorbing quaterrylenediimide chromophore for photoacoustic imaging and efficient photothermal cancer therapy, Angew. Chem. Int. Ed Engl. 58 (6) (2019) 1638–1642.

[43] Y. Qian, S. Qiao, Y. Dai, G. Xu, B. Dai, L. Lu, X. Yu, Q. Luo, Z. Zhang, Molecular-targeted immunotherapeutic strategy for melanoma *via* dual-targeting nanoparticles delivering small interfering RNA to tumor-associated macrophages, ACS Nano 11 (9) (2017) 9536–9549.